

Non-invasive thermal imaging of cardiac remodeling in mice

RAFAEL Y. BRZEZINSKI,^{1,2}  ZEHAVA OVADIA-BLECHMAN,³ NIR LEWIS,^{1,2} NETA RABIN,⁴ YAIR ZIMMER,³ LAPAZ LEVIN-KOTLER,^{1,2} OLGA TEPPER-SHAIHOV,^{1,2} NILI NAFTALI-SHANI,^{1,2} OLGA TSOREF,^{1,2} EHUD GROSSMAN,^{1,5} JONATHAN LEOR,^{1,2,*} AND OSHRIT HOFFER⁶

¹Sackler Faculty of Medicine, Tel Aviv University, Tel Aviv, 6997801, Israel

²Neufeld Cardiac Research Institute, Sackler Faculty of Medicine, Tel Aviv University, Israel; Tamman Cardiovascular Research Institute, Leviev Heart Center, Sheba Medical Center, Tel Hashomer, 52621, Israel

³School of Medical Engineering, Afeka Tel Aviv Academic College of Engineering, Tel Aviv, 6910717, Israel

⁴Department of Industrial Engineering, Tel-Aviv University, Tel Aviv, 6997801, Israel

⁵Internal Medicine Wing, and Hypertension Unit, Sheba Medical Center, Tel Hashomer, 52621, Israel

⁶School of Electrical Engineering, Afeka Tel Aviv Academic College of Engineering, Tel Aviv, 6910717, Israel

*leorj@post.tau.ac.il

Abstract: Thermal infrared imaging has been suggested as a non-invasive alternative to monitor physiological processes and disease. However, the use of this technique to image internal organs, such as the heart, has not yet been investigated. We sought to determine the ability of our novel thermal image-processing algorithm to detect structural and functional changes in a mouse model of hypertension and cardiac remodeling. Twelve mice were randomly assigned to receive either the pro-inflammatory, hypertensive hormone angiotensin-II (2 mg/kg/day, n = 6) or saline (n = 6) infusion for 28 days. We performed weekly blood pressure measurements, together with serial trans-thoracic echocardiography studies and histopathological evaluation of the hearts. Thermal images were captured with a commercially available thermal camera, and images were processed by our novel algorithm which analyzes relative spatial temperature variation across the animal's thorax. We assessed cardiac inflammation by measuring inflammatory cell infiltration through flow cytometry. Angiotensin infusion increased blood pressure together with cardiac hypertrophy and fibrosis. Thermal imaging at day 28 of the experiment detected an increase in the fraction of the skin heated by the heart in angiotensin-treated mice. Thermal image findings were significantly correlated to left ventricular volume and mass parameters seen on echocardiography ($r = 0.8$, $p < 0.01$ and $r = 0.6$, $p = 0.07$). We also identified distinct changes in the spatial heat profiles of all angiotensin-treated hearts, possibly reflecting remodeling processes in the hypertensive heart. Finally, a machine learning based model using thermal imaging parameters predicted intervention status in 10 out of 11 mice similar to a model using echocardiographic measurements. Our findings suggest, for the first time, that a new thermal image-processing algorithm successfully correlates surface thermography with cardiac structural changes in mice with hypertensive heart disease.

© 2019 Optical Society of America under the terms of the [OSA Open Access Publishing Agreement](#)

1. Introduction

Small animals are the most widely used laboratory animals for cardiovascular research. Current cardiovascular imaging modalities, such as small animal echocardiography and magnetic resonance imaging (MRI), are costly and require training and expertise for operation and interpretation of data.

Thermal infrared imaging is a non-invasive tool with the potential to screen physiological processes and disease [1]. Previous reports on thermal imaging in physiology and medicine have focused on inflammatory diseases, such as rheumatic diseases, that produce strong thermal manifestation in the skin [2,3]. Furthermore, non-invasive monitoring of changes in peripheral circulation by thermal imaging has been reported to reflect both local and systemic hemodynamic processes [4–9], especially in patients with cardiovascular disease [6,10–13]. However, the feasibility and usefulness of non-invasive thermal imaging to investigate internal organs, such as the heart, have not yet been investigated.

Here, we have developed a new image-processing tool that is based on images captured on a commercially available thermal camera. Our image-processing algorithm measures relative spatial temperature variation and consists of four main steps: 1) pre-processing; 2) filtering of thermal images of the heart; 3) feature extraction, and 4) production of a quantitative and qualitative estimation of cardiac structure.

We aimed to determine whether our technique could detect structural and functional changes in a mouse model of cardiac remodeling, and compare these findings to those seen on echocardiography. The ability to detect and monitor cardiac remodeling using a simple, accessible and inexpensive tool, could open up new experimental and clinical opportunities to advance our ability to screen and detect adverse cardiac remodeling and heart failure.

2. Materials and methods

2.1. Angiotensin-II infusion model

All animal experiments complied with the standards stated in the Guide for the Care and Use of Laboratory Animals (Institute of Laboratory Animal Resources, National Academy of Sciences) and were approved by the Sheba Medical Center Institutional Animal Care and Use Committee.

We implanted osmotic mini-pumps (Alzet, model: 1004) into 12-week old C57BL/6 male mice. Mice were anesthetized by inhalation of 2% isoflurane and 98% O₂. Then, pumps were inserted subcutaneously at the mid-scapular region. Twelve mice were randomly assigned to receive either the pro-inflammatory, hypertensive hormone angiotensin-II (2 mg/kg/day, n = 6) or saline (n = 6) infusion for 28 days. We performed weekly blood pressure measurements using a non-invasive volume/pressure tail-cuff device (Kent Scientific, Torrington, CT, USA) as previously described [14].

2.2. Echocardiography

To assess left ventricular (LV) remodeling and function, we performed transthoracic echocardiography with a special small animal echocardiography system (Vevo 2100 Imaging System; VisualSonics, Toronto, Ontario, Canada) equipped with a 22- to 55-MHz linear-array transducer (MS550D MicroScan Transducer, VisualSonics, Toronto, Ontario, Canada). Echocardiographic studies were performed before pump implantation, and at day 28 of the experiment. Light anesthesia was induced by inhalation of 2% isoflurane and 98% O₂, and subsequently maintained by 0.5% to 1% isoflurane. We controlled the isoflurane flow to maintain the heart rate at >400 bpm. Mice were fixed to an echocardiogram measuring platform heated to 37 C° during the test. All measurements were averaged for 3 consecutive cardiac cycles and performed by an experienced technician who was blinded to the treatment groups.

2.3. Thermal imaging

Thermal images were captured immediately before the beginning of the echocardiography study. Anesthesia was induced as described above and the images were captured using a FLIR One thermal camera device (FLIR Systems, Inc. Wilsonville, OR, USA) [15]. FLIR One utilizes the following functions: a frame rate frequency of 8.7Hz, an object temperature range of -20°C to

120°C, and thermal sensitivity of 150 mK. The wavelength sensitivity, over which the camera interpolates temperature, is 8–14 μm and the emissivity value considered appropriate for the animal for accurate temperature readings was 0.98. Image size was 480*640 (X by Y pixels) and the image field of view was 9.7cmX12.9cm. Images were taken at a distance of 10 cm, immediately after the mouse was fixed to the echocardiogram platform, but before the start of the echocardiography procedure (Fig. 1). We acquired two images per mouse and selected the best one for downstream analysis.

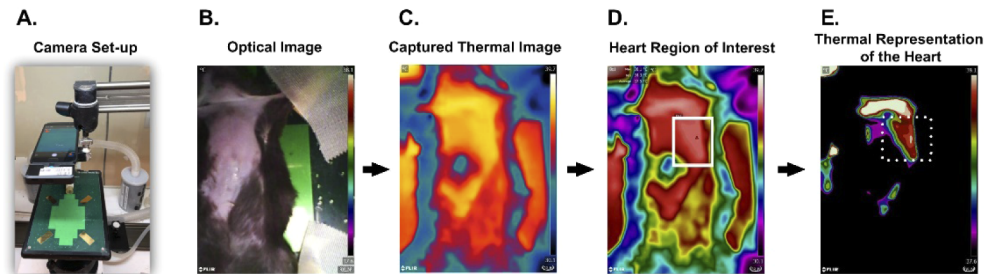


Fig. 1. Thermal Imaging Analysis Process: Images were captured by the commercially available FLIR One thermal camera device and analyzed using the FLIR Tools software. **A.** The camera connects to a smartphone placed 10 cm above the heated echocardiogram platform (37° C) to which the sedated mouse is fixed. **B.** An optical image of the sedated mouse. **C.** The captured thermal image (IRON scale). **D.** The same image as C in HC Rainbow scale. The region of interest representing the heart is marked (white square). **E.** The thermal image representing the heart (white dotted square) after reducing background noise according to temperature range (see details in Methods section).

2.4. Image processing

Thermal images were captured in two independent sessions, each leading to a different set of images. The first session was imaged 28 days after pump implantation ($n = 3$). For the images obtained in the first session, image processing was performed using the FLIR Tools software (Fig. 1).

We displayed the thermal image, with the region representing the heart being marked by a white square. The maximal temperature within the marked region was then extracted. We performed intensity-based thresholding focusing at a range of 0.5°C below the previously obtained maximal temperature. All the pixels outside this temperature range were changed to zero (black pixels). The obtained thermal image demonstrated a clear view of the heart which was segmented manually (Fig. 1). The area of the heart in the image (i.e. the number of image pixels representing the heart) was then computed from this image.

To assess changes in cardiac structure over time, we conducted a second experiment ($n = 3$) in which thermal images were captured at baseline and 28 days after pump implantation. In this second set of images, both room and whole animal (measured at the neckline) temperatures were lower than in the first experiment, and the above described image processing algorithm provided poor results. Therefore, we used an automated algorithm in order to extract the heart from the thermal image.

The range of temperature within the processed images was held constant at 0.5 °C and the same color map (HC Rainbow) was used for downstream processing. The algorithm first converts the thermal image from RGB to HSV representation. It then extracts the saturation channel (the variable S in the HSV color space). Most of the area displaying the mouse is colored in the original (RGB) image, while only the heart appears as a white region due to its high temperature. Accordingly, in the saturation image, the heart is darker than the rest of the mouse's body. After

extracting the S channel, the algorithm enables the user to select a region (containing the heart) from this image. The selected region is then negated, leading to an image containing the heart as bright pixels, and its vicinity as a darker background. The obtained image is segmented using the two-level Otsu method [16,17]. In order to eliminate small bright objects the obtained binary image is then smoothed using a morphological opening with a 7×7 -pixel square-shaped structuring element. The resulting image is displayed to the user. The area of the Otsu-segmented binary image of the thresholded inverted saturation map was used to quantify the heated skin area overlaying the heart. We also evaluated spatial heat profiles by measuring the roundness of the heart using the compactness shape feature. The compactness of an object is defined as: $C = \frac{P^2}{4\pi A}$ where P is the perimeter of the object and A is its area. The value of the compactness is lower for rounded objects and higher for elongated objects. The minimal possible value of the compactness is 1, and this value is obtained for a circle.

The algorithm was implemented using MATLAB software (Mathworks Inc. Natick, MA, USA). All image processing steps were done by researchers who were blinded to the treatment groups.

2.5. *Histopathologic evaluation*

At the end of the experiment (day 28) mice were euthanized by an over-dose inhalation of isoflurane. Hearts were perfused with 4% buffered formalin (Biolab), harvested, and sectioned into 2 transverse slices parallel to the atrioventricular ring. Each slice was embedded in paraffin, sectioned into 5- μ m slices, and stained with hematoxylin and eosin (H&E) and Masson Trichome's staining. Slides were photographed and analyzed with the use of planimetry software (Sigma Scan Pro version 5). We assessed perivascular fibrosis by calculating the perivascular fibrosis ratio i.e. the surrounding area of fibrosis around an artery divided by the total vessel wall thickness. An average of 3.1 arteries was measured in each heart.

2.6. *Flow cytometry*

To determine the levels of inflammatory cell infiltration to the heart, we analyzed total cell populations isolated from the hearts for common mouse monocyte and macrophage markers by flow cytometry. We isolated cells from the hearts of mice after 28 days of continuous angiotensin/saline infusion. Cells were extracted with an enzymatic digestion mixture as previously described [18] using 2 cycles of incubation at 37°C for 10 minutes. We analyzed the cells by flow cytometry using the fluorescent antimouse antibodies targeted towards CD11 and F4/80 (Biolegend). All samples were stained with the related isotype controls. We analyzed cells with a FACS Calibur cytometer (BD Bioscience) using the Flowjo Software (Tree Star).

2.7. *Statistical analysis and machine learning techniques*

Variables are expressed as mean \pm standard error of the mean (SEM). Specific statistical tests are detailed in the Figure legends. In brief, differences between values were tested by an unpaired t-test. If values were not normally distributed (tested by the D'Agostino Pearson omnibus normality test), we used the non-parametric Mann-Whitney test. We used 2-way repeated-measures analysis of variance (ANOVA) and Sidak's test for multiple comparisons to assess the significance of predefined comparisons at baseline and at day 28 of the experiment. To assess the correlation between the fraction of the skin heated by the heart and echocardiographic parameters, we used Pearson's test for normally distributed data and Spearman's test for an abnormal distribution. *P* values of <0.05 were considered statistically significant. All statistical analyses were performed with GraphPad Prism version 8.00 (GraphPad Software, La Jolla, CA, USA).

2.7.1. Machine learning based analysis

To further assess the diagnostic yield of our thermal imaging technique, we used a supervised machine learning classification method based on a support vector machine (SVM) algorithm [19]. SVM constructs a classification model of a given dataset in which the data points belong to one of two classes. The constructed model is then used to classify new data points. The input to the algorithm is a set of N data points denoted by $X = \{x_1, x_2, \dots, x_N\}$, where each data point consists of M descriptive values, $x_i = (x_{i,1}, x_{i,2}, \dots, x_{i,M})$. In addition, a binary label vector Y of size $N \times 1$, which holds the class (0/1) that is associated with each data point in X , is provided. Based on the input data points X and their associated classifications Y , a hyperplane that optimally separates the data points X , according to Y is calculated. The criterion for optimal separation used in SVM is that the distance from the separating hyper-plane to the nearest data point on each side is maximized. The classification $\bar{y} \in \{0, 1\}$ of a new data point $\bar{x} = (\bar{x}_1, \bar{x}_2, \dots, \bar{x}_M)$ can be predicted according to the relative location of \bar{x} from the hyperplane. Kernel-SVM [20] is a common extension to SVM. This extension relays on the *kernel trick* to separate the two classes of points in a nonlinear manner. The kernel maps the data into a higher-dimensional space, in which a separating hyperplane is computed. We used the radial basis function (RBF) kernel, which measures the pair-wise distance between a pair of data points by $w(x_i, x_j) = \exp\{-||x_i - x_j||^2/2\sigma\}$. The scale parameter σ controls the width of the radial kernel and it may be estimated heuristically from the pair-wise distances of X .

We used kernel-SVM to automatically predict the assigned treatment for each mouse (angiotensin/saline), according to the parameters calculated by our thermal imaging technique. Thermal imaging parameters on day 28 are assigned as input for the machine learning algorithm. Each mouse is characterized by 6 features: the size of the heart (in pixels), the heart's shape (assessed by compactness), heart temperature, body temperature, the difference between the body and the heart temperature, and the ratio between the body and heart temperature. Point classification is denoted by Y . Angiotensin infused mice are x_1, x_2, \dots, x_6 , and their labels y_1, y_2, \dots, y_6 are assigned to be 1. The saline-infused labels of each mouse x_7, x_8, \dots, x_{11} ($n = 5$) are set to be 0. Appendix Table 2 displays the input data matrix X with their correct classification labels Y .

The algorithm is executed in a leave-one-out cross-validation mode [21]. The algorithm is executed eleven times; in each execution, ten points from X , which correspond to 10 mice, are taken to be the input training set and one point from X (one mouse) is left out as the test point \bar{x} . In each of the eleven executions, a nonlinear surface is calculated in the 6-dimensional input space X and the new test point \bar{x} is inserted into the model. Its associated label \bar{y} is predicted according to the location of \bar{x} with respect to the hyper-plane (above/below). Finally, the results are evaluated by comparing the predicted label \bar{y} to the true label of the tested mouse. The results are reported using a confusion matrix that compares between the labels predicted by kernel-SVM and the true labels. An angiotensin-infused mouse that was misclassified as a saline-infused mouse is considered a type II error, referred to as false negative. A misclassification of the opposite type, in which a saline-infused mouse is predicted by kernel-SVM to be angiotensin infused, is referred to as a false positive error of type I.

To further evaluate the importance of specific thermal features, the SVM framework was executed on subsets of the six investigated features. We conducted five such experiments. The first subset consisted of four features: the size of the heart (in pixels), the heart's shape (compactness), heart temperature and body temperature. The second subset contained only two features: heart temperature and body temperature. The third subset consisted of four features: heart size, heart shape, the difference between the body and the heart temperature, and the ratio between the body and heart temperatures. The fourth subset contained two features: the difference between the body and the heart temperature, and the ratio between the body and heart temperature. The fifth subset contained two features: heart size and compactness. The evaluation of the kernel-SVM

framework for each input subset configuration was carried out in a leave-one-out cross-validation manner and the results are reported by using a confusion matrix.

To compare the diagnostic yield of thermal imaging with echocardiography, we applied the exact same kernel-SVM framework using echocardiographic measurements as input for the algorithm instead of thermal imaging measurements. Echocardiographic parameters were measured manually by the performing technician using the Vevo 2100 Imaging System software (VisualSonics, Toronto, Ontario, Canada). We included all standard parameters used for the assessment of cardiac structure (i.e. LV volume, mass and wall thickness) along with cardiac function (i.e. ejection fraction and fractional shortening) as previously described [18]. Parameters were computed for each mouse and formed a new dataset denoted by X, to be evaluated by the kernel-SVM framework (Table 3 in the Appendix).

3. Results

3.1. *Angiotensin increased blood pressure and adverse cardiac remodeling*

First, we sought to establish a robust model of cardiac hypertrophy and fibrosis in order to assess the ability of our imaging technique to detect cardiac remodeling. Angiotensin infusion increased blood pressure within 2 weeks of treatment. Systolic blood pressure increased from 110 ± 7 to 151 ± 11 mm Hg vs. 111 ± 4 to 115 ± 3 mm Hg in control animals ($p = 0.06$). Transthoracic echocardiography confirmed the development of cardiac hypertrophy and remodeling in angiotensin-treated mice compared with controls. We found a significant increase in LV mass and volume alongside increased aortic root dilation (Fig. 2).

Histopathologic evaluation of dissected hearts revealed that angiotensin induced larger areas of perivascular fibrosis compared with controls (Fig. 2). Perivascular fibrosis is a typical feature of hypertensive heart disease and associated inflammation. Taken together, these findings indicate that angiotensin induces cardiac hypertrophy and fibrosis in mice.

3.2. *Thermal imaging parameters correlate with cardiac remodeling*

Next, we sought to assess whether our thermal imaging process is able to visualize the murine-heart and detect the angiotensin-related cardiac structural changes seen on echocardiography.

Thermal image analysis at day 28 of the experiment detected an increase in the fraction of the skin heated by the heart (measured in pixels) in angiotensin-treated mice (Fig. 3). This increase possibly implicates an increase in cardiac mass or volume that leads to a wider scatter-pattern of heat. These findings were significantly correlated with LV volume and mass parameters seen on echocardiography ($r = 0.8$, $p < 0.01$ and $r = 0.6$, $p = 0.07$).

Besides an increase in size, angiotensin-treated hearts demonstrated a different shape of heat distribution compared with saline-infused mice. All hearts displayed a unique triangle-like shape, possibly reflecting remodeling processes in the hypertensive heart (Fig. 3).

These findings provided initial proof that our thermal camera and subsequent image processing were directly correlated with cardiac structural changes in mice.

3.3. *Thermal imaging correlates with the development of cardiac hypertrophy over time*

Next, we sought to evaluate changes in thermal imaging and cardiac remodeling over time. The 2nd experiment included thermal analysis and echocardiography at baseline and on day 28. We found that the fraction of the skin heated by the heart in angiotensin-treated mice increased by 430% at day 28 (Fig. 4). These findings once again correlated with the hypertrophy-related features on echocardiography, supporting the reproducibility of our technique (Fig. 5).

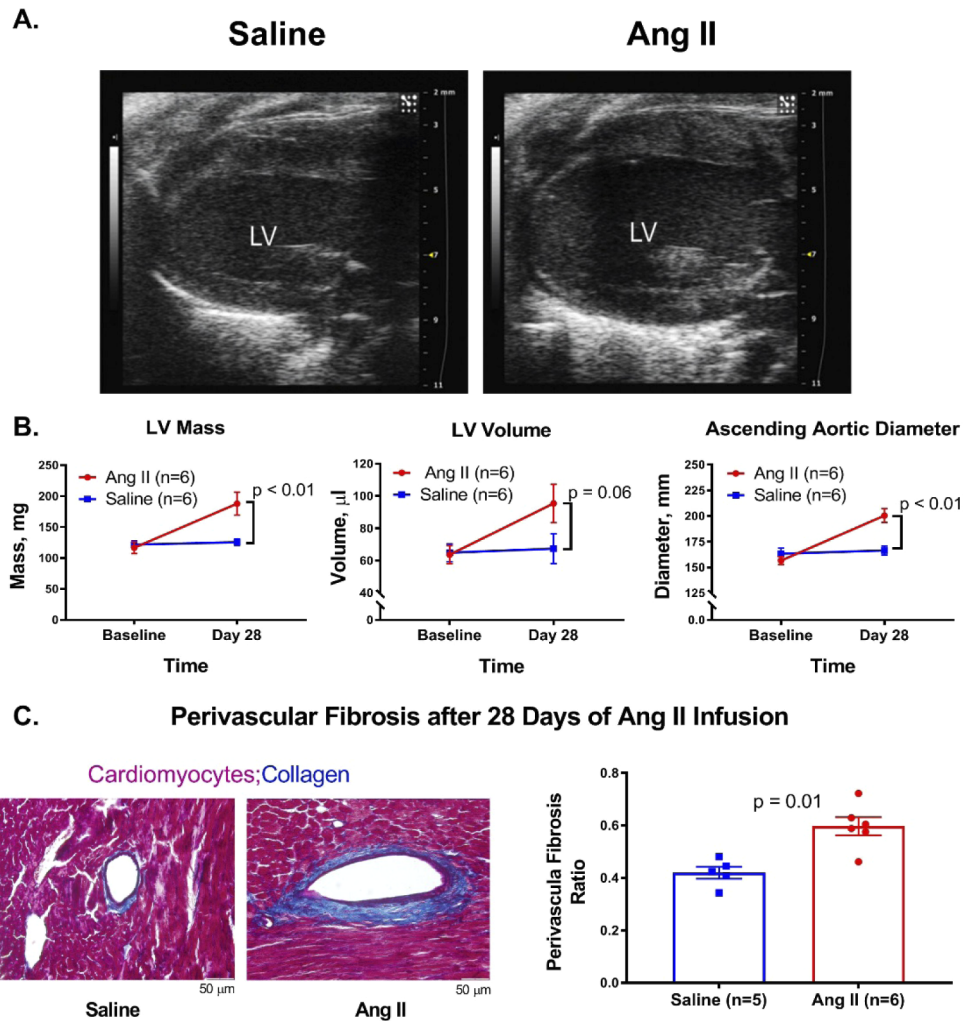


Fig. 2. Angiotensin Infusion Induces Cardiac Hypertrophy and Remodeling: We sought to evaluate the cardiac effects of continuous angiotensin infusion (2 mg/kg/day) for 28 days. **A-B.** We assessed cardiac structural changes over time via transthoracic echocardiography. **A.** Images show a parasternal long-axis view of the left ventricle (LV). Angiotensin-treated hearts (left) are dilated compared with control mice (right). **B.** The graphs display representative parameters indicating cardiac hypertrophy and remodeling. Data are shown as mean \pm SEM. P values were calculated by a two-way repeated measure ANOVA followed by Sidak's test for multiple comparisons. **C.** At the end of the experiment (day 28), hearts were stained with Masson's Trichrome staining and analyzed using planimetry software. Coronary perivascular fibrosis was assessed as the surrounding fibrotic area divided by the whole vessel wall. Angiotensin infusion significantly increased perivascular fibrosis. Data are shown as mean \pm SEM with individual measurements. P value was calculated by a Mann-Whitney test. Representative pictures of the stained blood vessels are shown. Ang II- Angiotensin II

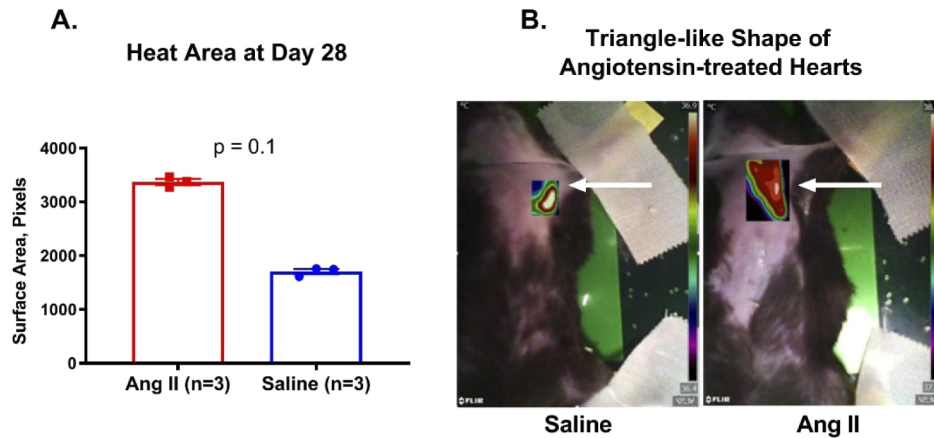


Fig. 3. Thermal Imaging Detects Cardiac Structural Changes: In the first round of the experiment ($n = 3$), we captured thermal images on day 28 (an average of 2 pictures per mouse). Images were processed as described in the Methods section. We measured the fraction of the skin heated by the heart (in pixels). **A.** Angiotensin-treated hearts were larger than saline controls. Data are shown as mean \pm SEM. P value was calculated by a Mann-Whitney test. **B.** Interestingly, the hearts from the angiotensin group all displayed a unique triangle-like shape of heat distribution that was not seen in the saline group. Representative images are shown in B; the thermal image of the hearts is placed on top of the optical image according to the region of interest processed by our algorithm (white arrow). Ang II- Angiotensin II

Heat Area Over Time

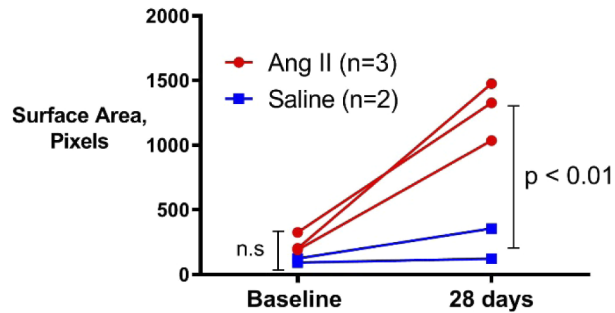


Fig. 4. Thermal Imaging of Cardiac Hypertrophy over Time: To assess thermal imaging and cardiac remodeling over time, the second experiment consisted of images captured at baseline and after 28 days. The area of heat over the heart of angiotensin-treated mice was increased by 430% on day 28. These differences were not significant at baseline. Individual measurements are presented. P values were calculated by a two-way repeated measure ANOVA followed by Sidak's test for multiple comparisons. Ang II- Angiotensin II

3.4. Machine learning classification methods yield similar predictive values in thermal and echocardiographic based models

We also assessed the diagnostic yield of our thermal imaging technique through the use of machine learning techniques. We applied kernel-SVM 11 times, in a leave-one-out cross-validation manner, to automatically predict the assigned treatment for each mouse (angiotensin/saline)

Correlation between Thermal Imaging and Echocardiography

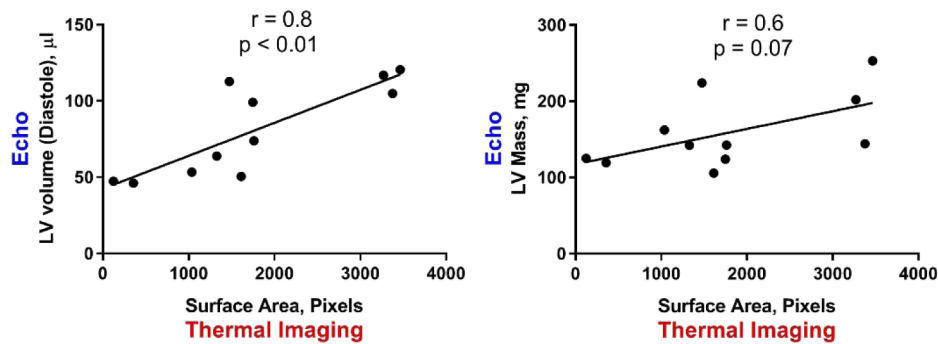


Fig. 5. Thermal Imaging Parameters Correlate with Echocardiographic Findings:

We sought to evaluate the correlation of our findings with parameters of echocardiography indicating cardiac hypertrophy. Cumulative data from both rounds ($n = 6$) demonstrated a significant correlation between heart size estimated by thermal imaging (measured in pixels), and echocardiographic measurements of both left ventricular volume (left) and mass (right). Data are shown as individual points with a linear trend. P values were calculated by Pearson's test. LV- Left ventricle

according to thermal imaging parameters. In each execution 10 mice were used as a training set for constructing the kernel-SVM model and the eleventh mouse was used as a test point. Ten of the 11 mice were classified correctly by the kernel-SVM algorithm (Table 1+ Appendix Table 2). The only misclassified mouse was an actual saline-infused mouse that demonstrated higher heart and whole body temperatures compared with other saline-treated mice (Table 2 in the Appendix).

Table 1. Confusion matrix for kernel-SVM classification based on all extracted thermal features

		Predicted label	
		Saline (0)	Angiotensin (1)
True label	Saline (0)	4	1
	Angiotensin (1)	0	6

To analyze the effect of specific subsets of calculated thermal features, we executed kernel-SVM four additional times excluding different subsets of parameters in each run (Tables 4–7 in the Appendix). Besides using all six thermal features, the combination of heart size and shape (compactness) best differentiated between angiotensin and saline-infused mice (9 out of 11 mice were classified correctly using this subset, Table 7 in the Appendix).

Next, we aimed to compare the predictive capabilities of the model when using thermal imaging features as opposed to using echocardiography-based parameters. Nineteen echocardiographic measurements were used as input for the kernel-SVM framework (Table 3 in the Appendix). The resulting confusion matrix was identical to the one generated by thermal-based measurements (Table 1). The misclassified mouse was the same mouse that was misclassified as false positive when using the thermal-based model. Overall, thermal imaging yielded the same prediction rate compared with standard echocardiography.

3.5. Angiotensin did not increase inflammation in the heart after 28 days

Finally, to test the hypothesis that the observed changes in thermal imaging were related to the degree of local inflammation in angiotensin-treated hearts, we measured inflammatory cell

infiltration to the heart by flow cytometry. Angiotensin did not significantly increase monocyte (CD11⁺) and macrophage (F4/80⁺) infiltration to the heart at day 28 of the experiment. (Fig. 6). These low levels of innate immune cells suggest a relatively low degree of cardiac inflammation 28 days after pump implantation.

Monocyte/ Macrophage accumulation in the Heart

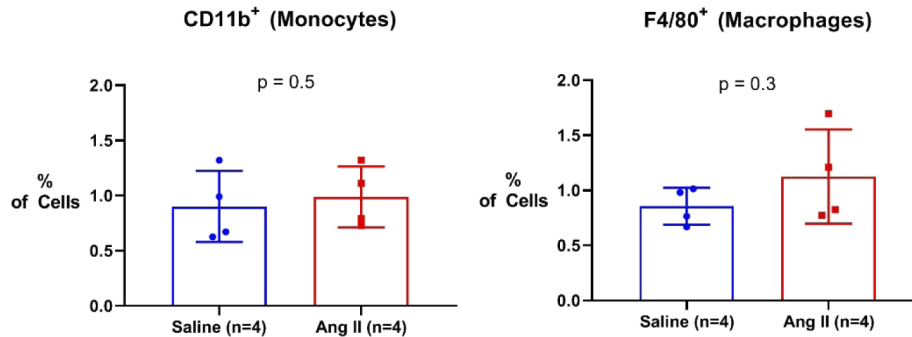


Fig. 6. Angiotensin infusion does not elevate local inflammation after 28 days: We measured innate inflammatory cell infiltration to the heart by flow cytometry. We isolated cells from the hearts of mice after 28 days of angiotensin/saline infusion. Hearts of angiotensin-treated mice did not have elevated levels of monocytes (CD11⁺, left) or macrophages (F4/80⁺, right). P values were calculated by an ordinary two-way ANOVA with Sidak's test for multiple comparisons.

4. Discussion

Our findings suggest, for the first time, that a thermal camera using a new image-processing algorithm could potentially be used to study cardiovascular diseases in mice. Thoracic thermodynamic features were directly correlated with angiotensin-related cardiac hypertrophy and remodeling seen on small-animal echocardiography (Fig. 7). To our knowledge, this is the first report to describe the use of a standard commercially available thermal imaging device to image cardiac structural abnormalities in mice.

This potential imaging technique has several advantages over currently available alternatives. First, the capturing of images is simple, quick and does not require technical training compared to echocardiography. Second, our image processing algorithm is suitable for a variety of commercially available thermal cameras, making it potentially affordable for laboratory use worldwide. Of note, our algorithm was able to detect cardiac structural changes despite relatively low sensitivity and resolution levels of the FLIR One camera device. Future studies on higher performing thermal imaging devices might present an even higher diagnostic yield. Finally, the FLIR One camera used by us is portable and connects directly to a variety of smartphones. Potential future use in humans could enable rapid and close monitoring of disease progression, various treatments, and associated biomarkers with relatively reduced effort and time. Further development of this technique could possibly also improve follow-up of home-care patients.

Previous reports have demonstrated the potential use of thermal imaging in the detection of vascular inflammation and vulnerable atherosclerotic plaques [22,23]. Our method is the first to report marked structural changes in the remodeled murine-heart due to pressure-induced hypertrophy and fibrosis. Possible combinations of these techniques could lead to significant progress in the field of thermal cardiovascular imaging.

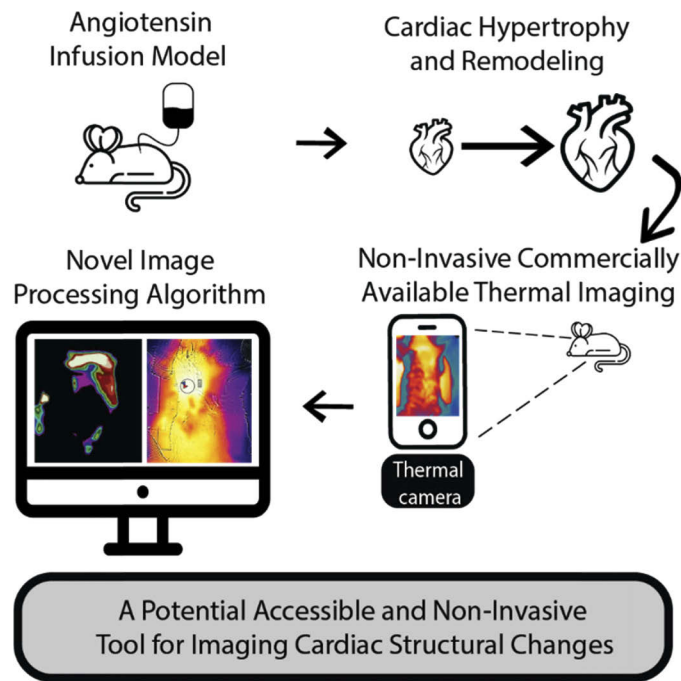


Fig. 7. Summary Fig.: A graphic scheme describing our new non-invasive tool for imaging structural changes in diseased hearts.

The use of thermal imaging has several inherent limiting aspects. It is strongly influenced by environmental factors such as room temperature, working surface temperature and manual handling of the animal. Accordingly, future experiments should include test settings that try and standardize these factors as much as possible. The significant differences in working temperatures limited our ability to compare between the absolute numbers of pixels in each round of the experiment. Nevertheless, the image findings on both rounds showed similar patterns and sensitivity levels, identifying this method as reproducible and thus suitable for future evaluation. Our algorithm performs automatic thresholding and appears to yield more informative results than simply performing a manual intensity-based thresholding of thermal images. It should be noted that both absolute heart temperatures and heart/body temperature ratios were not significantly different between the two experimental groups Table 2 in the Appendix. A detailed analysis of the gradient of temperature distribution and other spatial-thermal data extracted from images could improve the predictive power of this imaging tool. Further adjustments and validation of our algorithm are still needed to enable standardization between experiments. Finally, our relatively small sample size limited the amount of validation of our SVM prediction model.

Our findings relate to two main aspects of the hypertensive heart [24]: the first being an increase in size, and the second the altered shape of heat distribution, possibly indicating cardiac remodeling (Fig. 3). The biological explanation for these observed changes is not entirely clear. We hypothesize that the increase in LV blood volume plays a key role in the thermal energy emitted by the remodeled heart. Elevated thermal energy ultimately leads to heating of the skin surface which is visible on the thermal imaging device. Furthermore, an increase in the myocardial mass might have led to the observed changes in the shape of heat manifestation in the skin. Our findings are in line with a recent report by van Nierop et al. [25] who evaluated cardiac hypertrophy in mice by cardiac MRI. Diseased hearts had a different orientation in the long-axis view that resembled the triangle-like shape of heat observed when using our thermal

imaging technique. Finally, cardiac and vascular inflammation could also be the source of the elevated heat captured by our thermal camera. However, in light of the relatively low degree of local inflammation measured on day 28 of the experiment (Fig. 6), it seems the change in cardiac blood volume had a greater effect on the thermal signal captured by our device. Additional models of cardiac disease with elevated degrees of inflammation such as myocardial infarction and myocarditis need to be examined in future studies.

4.1. Conclusions

The use of a commercially available thermal camera with our new image processing algorithm is potentially useful for screening cardiac structural changes in mice. Future developed versions of this tool could be used to evaluate and monitor new therapies for cardiac remodeling. Our findings stimulate future studies to assess the potential use of thermal imaging in humans and other animal models of diseases.

Appendix

Table 2. Thermal-based input data set X for kernel-SVM along with the corrected and predicted classification vector Y

	Heart size, pixels	Heart Com- pactness	Heart Temp. °C	Body Temp. °C	Body-Heart Temp. difference	Body/ Heart Temp. ratio	Label y_i	Predicted Label \bar{y}
x_1	3377	1.76	37	37.1	0.1	1.003	1	1
x_2	3270	2.34	36.3	35.1	-1.2	0.967	1	1
x_3	3466	2.59	38.1	38.3	0.2	1.005	1	1
x_4	1327	3.28	37.3	37.4	0.1	1.003	1	1
x_5	1475	2.95	34.7	34.3	-0.4	0.988	1	1
x_6	1036	1.51	34.9	35.1	0.2	1.006	1	1
x_7	1612	1.55	35.4	34.8	-0.6	0.983	0	0
x_8	1748	2.02	36.1	35.4	-0.7	0.981	0	0
x_9	1760	1.93	36.9	37.1	0.2	1.005	0	0
x_{10}	356	2.42	36.9	36.4	-0.5	0.986	0	0
x_{11}	123	1.88	37.4	37.6	0.2	1.005	0	1

Temp.- Temperature

Table 3. Echocardiography-based input data set X for kernel-SVM along with the corrected and predicted classification vector Y

	x_1	x_2	x_3	x_4	x_5	x_6	x_7	x_8	x_9	x_{10}	x_{11}
Ascending aortic diameter, mm	1.949354	2.239207	2.154032	1.927136	1.959473	1.793878	1.668399	1.681814	1.813984	1.48555	1.624713
Ascending aortic thickness, mm	0.13019	0.111364	0.123767				0.101765	0.137826	0.102478		
Diastolic endocardial area, mm ²	14.82607	18.21204	18.35143	13.01051	21.139	11.63391	8.407376	12.95404	12.32753	11.86676	9.149479
Systolic endocardial area, mm ²	9.442019	12.01166	13.76074	9.851492	12.23673	5.047265	4.019841	9.915679	7.86854	6.031581	3.478566
Diastolic interventricular septal wall thickness, mm	0.761921	0.885464	1.048975	1.181041	1.068716	1.217914	0.896593	0.692771	0.914063	1.048468	1.051007
Systolic interventricular septal wall thickness, mm	1.107422	1.265818	1.441551	1.551563	1.381159	1.575737	1.284142	0.776357	1.172099	1.361535	1.554156
Diastolic LV internal dimension, mm	4.747042	4.974204	5.039083	3.848586	4.898689	3.568301	3.486446	4.635531	4.090169	3.360079	3.395502
Systolic LV internal dimension, mm	3.697927	3.875684	4.101637	3.392096	3.600332	2.304912	2.186143	3.901337	3.170134	2.480675	2.219652
Diastolic posterior wall thickness, mm	0.738417	0.942919	1.078174	0.738524	0.944723	1.054935	0.843874	0.682774	0.879024	0.918318	0.957953
Systolic posterior wall thickness, mm	1.037208	1.187603	1.271686	0.684461	1.230571	1.426609	1.271893	0.833432	1.142666	1.087701	1.231057
b;d	2.172392	2.407711	2.416908	2.035037	2.593984	1.924367	1.635895	2.030615	1.980903	1.94353	1.706567
LV ejection fraction, %	44.59488	44.41874	38.29593	26.13362	51.70995	65.81168	68.35592	33.44111	45.75004	52.50918	64.95513
Endocardial Area Change, mm ²	5.38405	6.200381	4.590689	3.159022	8.902267	6.586645	4.387535	3.038356	4.458989	5.83518	5.670913
Endocardial fractional area change, %	36.31475	34.0455	25.01543	24.28053	42.113	56.61592	52.18674	23.4549	36.17099	49.17247	61.98072
LV fractional shortening, %	22.10039	22.08434	18.6035	11.86124	26.50417	35.4059	37.29595	15.8384	22.49381	26.17212	34.62964
LV Mass	144.1156	201.8767	252.7903	142.062	223.9622	162.0146	105.7461	123.8217	142.375	119.2172	124.9979
LV Mass (Corrected)	115.2925	161.5013	202.2323	113.6496	179.1698	129.6117	84.59691	99.05735	113.9	95.37373	99.99831
Diastolic LV Volume, ul	104.771	116.8298	120.4019	63.85867	112.7438	53.28829	50.39573	99.10593	73.8016	46.10182	47.28452
Systolic LV Volume, ul	58.04848	64.93548	74.29285	47.17009	54.44405	18.21837	15.94726	65.96381	40.03734	21.89413	16.5708
Label y_i	1	1	1	1	1	1	0	0	0	0	0
Predicted Label \hat{y}	1	1	1	1	1	1	0	0	0	0	1

LV- Left Ventricle

Table 4. Confusion matrix for kernel SVM classification based on absolute heart and body temperature

		Predicted label	
		Saline (0)	Angiotensin (1)
True label	Saline (0)	3	2
	Angiotensin (1)	1	5

Table 5. Confusion matrix for kernel SVM classification based on heart size, compactness, and body to heart temperature difference and ratio

		Predicted label	
		Saline (0)	Angiotensin (1)
True label	Saline (0)	4	1
	Angiotensin (1)	0	6

Table 6. Confusion matrix for kernel SVM classification based on body to heart temperature difference and ratio

		Predicted label	
		Saline (0)	Angiotensin (1)
True label	Saline (0)	3	2
	Angiotensin (1)	1	5

Table 7. Confusion matrix for kernel SVM classification based on heart size and compactness

		Predicted label	
		Saline (0)	Angiotensin (1)
True label	Saline (0)	4	1
	Angiotensin (1)	1	5

Acknowledgments

We thank Vivienne York for her skillful English-language editing of the manuscript. This work was performed in partial fulfillment of the requirements for a Ph.D. degree of Rafael Y. Brzezinski at the Sackler Faculty of Medicine, Tel Aviv University, Tel Aviv, Israel.

Disclosures

The authors declare that there are no conflicts of interest.

References

1. E. F. J. Ring and K. Ammer, "Infrared thermal imaging in medicine," *Physiol. Meas.* **33**(3), R33–R46 (2012).
2. I. Gannot, M. Ben-David, O. Hopper, M. Sholomov, E. Katz, and I. Kelson, "A portable thermal imaging device as a feedback system for breast cancer treatment," in *Optical Fibers and Sensors for Medical Diagnostics and Treatment Applications XVIII*, I. Gannot, ed. (SPIE, 2018), p. 27.
3. O. A. Hoffer, M. A. Ben-David, E. Katz, D. Zoltnik Kirshenabum, D. Alezra, Y. Zimmer, I. Kelson, and I. Gannot, "Thermal imaging as a tool for evaluating tumor treatment efficacy," *J. Biomed. Opt.* **23**(05), 1 (2018).
4. S. Bagavathiappan, T. Saravanan, J. Philip, T. Jayakumar, B. Raj, R. Karunanithi, T. M. R. Panicker, M. P. Korath, and K. Jagadeesan, "Infrared thermal imaging for detection of peripheral vascular disorders," *J. Med. Phys.* **34**(1), 43–47 (2009).
5. T. J. Love, "Thermography as an Indicator of Blood Perfusion," *Ann. N. Y. Acad. Sci.* **335**(1 Thermal Chara), 429–437 (1980).
6. Z. Ovadia-Blechman, I. Avrahami, E. Weizman-Shammai, T. Sharir, M. Eldar, and P. Chouraqui, "Peripheral microcirculatory hemodynamic changes in patients with myocardial ischemia," *Biomed. Pharmacother.* **74**, 83–88 (2015).
7. M. Lustig, A. Levy, K. Kopplin, Z. Ovadia-Blechman, and A. Gefen, "Beware of the toilet: The risk for a deep tissue injury during toilet sitting," *J. Tissue Viability* **27**(1), 23–31 (2018).
8. Z. Ovadia-Blechman, B. Gavish, D. Levy-Aharoni, D. Shashar, and V. Aharonson, "The coupling between peripheral microcirculation and slow breathing," *Med. Eng. Phys.* **39**, 49–56 (2017).
9. Z. Ovadia-Blechman, A. Gritzman, M. Shuvi, B. Gavish, V. Aharonson, and N. Rabin, "The response of peripheral microcirculation to gravity-induced changes," *Clin. Biomech.* **57**, 19–25 (2018).
10. J. A. Schmidt, C. Bracht, A. Leyhe, and P. von Wichert, "Transcutaneous measurement of oxygen and carbon dioxide tension (TcPO₂ and TcPCO₂) during treadmill exercise in patients with arterial occlusive disease (AOD)—stages I and II," *Angiology* **41**(7), 547–552 (1990).

11. Z. Ovadia-Blechman, A. Meilin, N. Rabin, M. Eldar, and D. Castel, "Noninvasive monitoring of peripheral microcirculatory hemodynamics under varying degrees of hypoxia," *Respir. Physiol. Neurobiol.* **216**, 23–27 (2015).
12. Z. Ovadia, R. Kornowski, B. Gavish, D. Chayen, R. Walden, N. Varda-Bloom, A. Battler, and M. Eldar, "Noninvasive evaluation of microcirculatory hemodynamic changes during hemorrhage followed by saline or blood transfusion," *Shock* **4**(2), 96–101 (1995).
13. P. Rao, J. B. Keenan, T. K. Rajab, A. Ferng, S. Kim, and Z. Khalpey, "Intraoperative thermographic imaging to assess myocardial distribution of Del Nido cardioplegia," *J. Card. Surg.* **32**(12), 812–815 (2017).
14. C. M. Haggerty, A. C. Mattingly, M. C. Gong, W. Su, A. Daugherty, and B. K. Fornwalt, "Telemetric Blood Pressure Assessment in Angiotensin II-Infused ApoE^{-/-} Mice: 28 Day Natural History and Comparison to Tail-Cuff Measurements," *PLoS One* **10**(6), e0130723 (2015).
15. Y. Cho, S. J. Julier, N. Marquardt, and N. Bianchi-Berthouze, "Robust tracking of respiratory rate in high-dynamic range scenes using mobile thermal imaging," *Biomed. Opt. Express* **8**(10), 4480 (2017).
16. P. K. Sahoo, S. Soltani, and A. K. C. Wong, "A survey of thresholding techniques," *Comput. Vision, Graph, Image Process.* **41**(2), 233–260 (1988).
17. N. Otsu, "A threshold selection method from gray level histogram," *IEEE Trans. Syst. Man Cybern.* **9**(1), 62–66 (1979).
18. N. Naftali-Shani, L.-P. Levin-Kotler, D. Palevski, U. Amit, D. Kain, N. Landa, E. Hochhauser, and J. Leor, "Left Ventricular Dysfunction Switches Mesenchymal Stromal Cells Toward an Inflammatory Phenotype and Impairs Their Reparative Properties Via Toll-Like Receptor-4," *Circulation* **135**(23), 2271–2287 (2017).
19. C. Cortes and V. Vapnik, "Support-Vector Networks," *Int. J. Mach. Learn. Cybern.* **20**(3), 273–297 (1995).
20. T. Hofmann, B. Schölkopf, and A. J. Smola, "Kernel methods in machine learning," *Ann. Stat.* **36**(3), 1171–1220 (2008).
21. S. Geisser, *Predictive Inference*. (Chapman and Hall, 1993).
22. M. Madjid, M. Naghavi, B. A. Malik, S. Litovsky, J. T. Willerson, and W. Casscells, "Thermal detection of vulnerable plaque," *Am. J. Cardiol.* **90**(10), L36–L39 (2002).
23. H. Kosuge, S. P. Sherlock, T. Kitagawa, R. Dash, J. T. Robinson, H. Dai, and M. V. McConnell, "Near Infrared Imaging and Photothermal Ablation of Vascular Inflammation Using Single-Walled Carbon Nanotubes," *J. Am. Heart Assoc.* **1**(6), e002568 (2012).
24. F. H. Messerli, S. F. Rimoldi, and S. Bangalore, "The Transition From Hypertension to Heart Failure," *JACC Hear. Fail.* **5**(8), 543–551 (2017).
25. B. J. van Nierop, H. C. van Assen, E. D. van Deel, L. B. P. Niesen, D. J. Duncker, G. J. Strijkers, and K. Nicolay, "Phenotyping of Left and Right Ventricular Function in Mouse Models of Compensated Hypertrophy and Heart Failure with Cardiac MRI," *PLoS One* **8**(2), e55424 (2013).